# Effects of O vacancies and N or Si substitutions on Li$^+$ migration in Li$_3$PO$_4$ electrolytes from first principles

Yaojun A. Du[*] and N. A. W. Holzwarth[†]

*Department of Physics, Wake Forest University, Winston-Salem, North Carolina 27109, USA*

As a first step toward optimizing solid-state electrolyte materials, we have constructed realistic models of various types of isolated defects in crystalline Li$_3$PO$_4$ involving O vacancies and N and Si dopants, and have used first-principles calculational methods to study their effects on the production and migration of mobile Li ions. We find that mobile Li-ion vacancies are stabilized by removing oxygen from the lattice, which, in turn, causes the rebonding of nearby phosphate groups to form O$_3$P-O-PO$_3$ (POP) structures embedded in the crystal. In the presence of nitrogen in the system, the POP structures can be further stabilized by replacing the bridging oxygen with nitrogen. We examine the electronic and geometric structures of these stable POP and O$_3$P-N-PO$_3$ (PNP) defects which are prototypes of chain structures found in thin-film lithium phosphorus oxynitride (LiPON) electrolytes. We also find that mobile interstitial Li ions are stabilized by N or Si dopants substituting for O or P host ions and forming PO$_3$N or SiO$_4$ defects, respectively. In all of these cases, the defect not only stabilizes extrinsic mobile ions but also provides traps for the ions to escape into the bulk regions of the crystal by as much as 1.5 eV for the vacancies and 0.9 eV for the interstitials. On the other hand, migration barriers for diffusion steps near the defects are as small as 0.4–0.6 eV for the vacancies and 0.2–0.3 eV for the interstitials. Extrapolating our results to crystals with appreciable concentrations of defects, we find that our results compare favorably with experimental migration energies reported in the literature.

## I. INTRODUCTION

In previous work,[1,2] we used first-principles modeling techniques to examine mechanisms for Li-ion diffusion in idealized crystals of Li$_3$PO$_4$, considering both vacancy and interstitial processes. The temperature ($T$)-dependent conductivity ($\sigma$) of these materials is characterized by a migration energy $E_m$ as expressed by the Arrhenius relation

$$\sigma T = Kne^{-E_m/k_BT}, \qquad (1)$$

where $n$ denotes the concentration of mobile ions, $K$ is a temperature-independent constant appropriate to the diffusion path, and $k_B$ denotes the Boltzmann constant. For the idealized crystals, the migration energy for vacancy diffusion via a direct hopping mechanism was found to be 0.6 eV $\leq E_m \leq 0.7$ eV, while the migration energy for interstitial diffusion via an interstitialcy mechanism was found to be 0.3 eV $\leq E_m \leq 0.5$ eV. The calculated results were in excellent agreement with experimental measurements[3] of thermally activated Li-ion conductivity in single-crystal $\gamma$-Li$_3$PO$_4$. The conductivity in these single crystals is very small because in this case, the concentration of mobile ions, $n$, is itself controlled by a thermally activated process, requiring a formation energy $E_f$. Therefore the perfect-crystal Arrhenius relation takes the form

$$\sigma_{\text{cry}} T = K' e^{-(E_f/2+E_m)/k_BT}, \qquad (2)$$

where $K'$ is a temperature-independent constant.

Consequently, in order to take advantage of the favorable migration energies $E_m$ for ionic conduction, it is necessary to construct Li$_3$PO$_4$ materials with an extrinsic concentration $n$ of mobile Li ions. The purpose of the present work is to construct realistic models of various types of isolated defects in crystalline Li$_3$PO$_4$, involving O vacancies and N and Si

dopants, and to study their effects on the production and migration of mobile Li ions. The study of Li-ion mobility in these well-defined structures is a step toward the development of optimized Li$_3$PO$_4$-based solid-state electrolyte materials for use in rechargeable batteries. For example, lithium phosphorus oxynitride ("LiPON") materials are under development at the Oak Ridge National Laboratory,[4–8] for a variety of applications including electrolytes for rechargeable Li-ion batteries. Having variable compositions which can be quantified as Li$_{3+x}$PO$_{4-y}$N$_z$, where the concentration variables must satisfy $x=3z-2y$ for neutral systems, the LiPON films have been demonstrated to have good Li-ion conductivity and excellent chemical and physical stability, particularly at their interfaces with cathodes and anodes. Another example of a solid electrolyte system is based on solid solutions of Li$_3$PO$_4$ and Li$_4$SiO$_4$ which have been studied by a few groups.[4,5,9–11] This system, while showing favorable conductivity properties, has received less experimental attention than LiPON, perhaps due to its reactivity with the Li anodes.[4,5]

The outline of the paper is as follows. In Sec. II, we describe the calculational methods. We then consider defects associated with Li-ion vacancies. It turns out that the most stable of these follows from the production of an O vacancy and the subsequent rebonding of two phosphate groups, as presented in Sec. III. In Sec. IV, we consider the effects of N substituting for O within a phosphate group, which stabilizes an interstitial Li ion. In Sec. V, we consider the effects of Si substituting for P, which also stabilizes an interstitial Li ion. In Sec. VI, our results are related to experimental measurements. A summary and conclusions are given in Sec. VII.

## II. CALCULATIONAL METHODS

In this study, we used the same calculational techniques as described in our earlier work[1,2] on crystalline Li$_3$PO$_4$. The

174301-1

calculations were based on density-functional theory[12,13] using the local-density approximation for the exchange-correlation functional.[14] The calculations were carried out using the QUANTUM ESPRESSO (PWSCF) package[15] with the ultrasoft-pseudopotential formalism[16] and also the PWPAW code[17,18] with the projector-augmented-wave formalism.[19,20] Visualizations of the structures were obtained using the XCRYSDEN (Ref. 21) and OPENDX (Ref. 22) software. Estimates of the migration energies $E_m$ for Li-ion diffusion were calculated using the nudged-elastic-band (NEB) method[23–25] as implemented in the PWSCF code. Most of the defect structures were based on 128-atom supercells of the perfect crystals, using the same optimized lattice constants and calculational parameters as described in our earlier work. For some of the simulations, slightly larger simulation cells were used. The majority of the simulations were based on the $\gamma$-Li$_3$PO$_4$ crystalline form which has the *Pnma* structure,[7,26–28] while a few simulations were also based on the $\beta$-Li$_3$PO$_4$ crystalline form which has the *Pmn*$2_1$ structure.[26,29] The defect structures were modeled within neutral supercells, starting with a reasonable initial structure and optimizing the structure at constant volume.

As in the LiPON materials, the stoichiometry of lithium phosphate doped with N can be expressed as Li$_{3+x}$PO$_{4-y}$N$_z$, where the concentration parameters must satisfy the relation $x = 3z - 2y$ in order to represent a neutral system. Both Li-ion vacancies ($x < 0$) and Li-ion interstitials ($x > 0$) can be obtained by varying the O and N concentrations. In this work, the vacancy simulations were modeled with $z = -x = y/2$ (Li$_{3-z}$PO$_{4-2z}$N$_z$). Calculations with $z = \frac{1}{16}$ and with $z = \frac{1}{24}$ were performed as described in Sec. III. Nitrogen-induced interstitials were modeled with $z = x = y$ (Li$_{3+z}$PO$_{4-z}$N$_z$). Calculations with $z = \frac{1}{16}$ were performed as described in Sec. IV. In addition, we modeled Si-induced interstitial materials with the general stoichiometry of Li$_{3+u}$Si$_w$P$_{1-v}$O$_4$, where in this case, the concentration parameters must satisfy the relation $u = 5v - 4w$ in order to represent a neutral system. Our simulations considered $u = v = w = \frac{1}{16}$ as described in Sec. V.

## III. DEFECTS CAUSING Li-ION VACANCIES

### A. Stable O$_3$P-N-PO$_3$ and O$_3$P-O-PO$_3$ defects

In both of the common crystalline forms of Li$_3$PO$_4$, the structure is characterized by tetrahedra of [PO$_4$]$^{-3}$ negative ions arranged among Li$^{+1}$ positive ions. The two crystals structures ($\gamma$ and $\beta$) differ primarily in the orientations of the phosphate tetrahedra. In order to produce a Li-ion vacancy in this material while maintaining charge neutrality, an O ion must be removed from a PO$_4$ group in the lattice. For isolated neutral clusters, we find that PO$_4$ stabilizes in a tetrahedral structure, while PO$_3$ stabilizes in a threefold planar structure. In crystalline $\gamma$- and $\beta$-Li$_3$PO$_4$, there are three inequivalent O positions in each of the $\gamma$ and $\beta$ structures. We find that removing one type of O results in the formation of an approximately planar PO$_3$ defect, consistent with the isolated phosphite simulations, while removing either of the other two types of O results in a much more stable defect (by approximately 1.7 eV) characterized by rebonding of neigh-
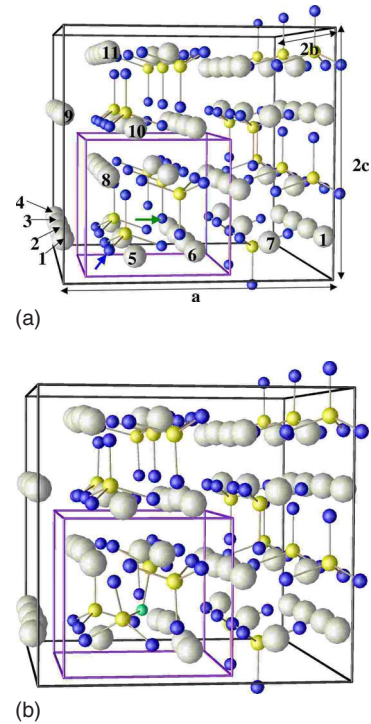


FIG. 1. (Color online) Ball-and-stick diagram of $\gamma$-Li$_3$PO$_4$ supercell indicating PO$_4$ groups with bonded yellow and blue spheres and Li ions with gray spheres. Diagram (a) shows the perfect crystal. The numbers on the Li sites indicate vacancy positions studied. Blue or green arrows indicate the sites where O will be removed or replaced with N, respectively, to form the relaxed "bent" PNP defect structure shown in (b), with the N site indicated with a green sphere. The purple rectangular frame indicated in both diagrams represents the volume drawn in Fig. 3.

boring phosphate groups to form O$_3$P-O-PO$_3$ (POP). Here the central O is bonded to two P ions in what can be thought of as a bridging structure.

For example, Fig. 1(a) shows a perfect $\gamma$-Li$_3$PO$_4$ supercell with an arrow indicating the oxygen that can be removed to form a relaxed bent defect structure similar to that shown Fig. 1(b). Similarly, Fig. 2(a) shows a perfect $\gamma$-Li$_3$PO$_4$ supercell with an arrow indicating a different oxygen that can be removed to form a relaxed straight defect structure similar to that shown in Fig. 2(b).

For both of the bent and straight rebonded phosphate structures, the system can be further stabilized by replacing the "bridging" O ion with a N ion. Considering supercells with the stoichiometry of Li$_{3-1/16}$PO$_{4-2/16}$N$_{1/16}$ and fixing the Li vacancy position, we find that relaxed structures with N at the bridging site have a lower energy by nearly 3 eV compared to relaxed structures with N replacing a tetrahedral phosphate O.[30] The relaxed bent PNP structure shown in Fig. 1(b) corresponds to the lowest-energy configuration of this defect in this supercell, with the Li-ion vacancy at site labeled 5 in Fig. 1(a). The relaxed straight PNP structure in Fig. 2(b) corresponds to the lowest-energy configuration of this defect in this supercell with the Li-ion vacancy at site labeled 2 in Fig. 2(a). Defect structures formed with O and Li vacancies in $\beta$-Li$_3$PO$_4$ are very similar to those presented
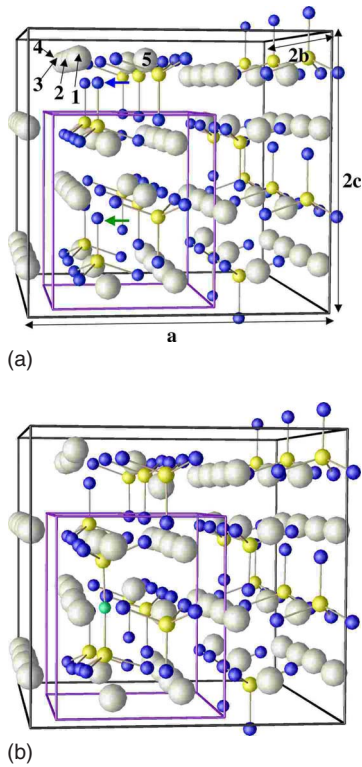
FIG. 2. (Color online) Similar diagrams to those in Fig. 1. The blue and green arrows in the perfect-crystal diagram in (a) indicate different O sites which result in the "straight" PNP defect structure shown in (b). The purple rectangular frame indicated in both diagrams represents the volume drawn in Fig. 4.

here. Some of the corresponding structural diagrams are given in the supplemental materials.[31] Diagrams of the $O_3P-N-PO_3$ ("PNP") and "POP" defects within the indicated section of the supercell are shown in Figs. 3 and 4 for the bent and straight structures, respectively. Also indicated in these diagrams are contour plots of the electron valence densities plotted on the P-N-P and P-O-P planes. From these

diagrams, it is clear that PNP and POP defects have very similar geometric and electronic structures.

Partial-density-of-states analyses provide qualitative information on the states involved with the bridging N and O ions in relation to the other states of the material. Plots of the partial densities of states are shown in Fig. 5, comparing the results for the bent PNP and POP structures with those of the ideal supercell. In this figure, the partial densities of states for the bridging -N- and -O- sites are presented separately. Interestingly, the densities of states spectra shown in Fig. 5 are very similar to those found for the straight PNP and POP structures and for the corresponding structures derived from $\beta$-$Li_3PO_4$ crystals, as shown in the supplemental materials of this paper.[31] The most striking feature of the PNP and POP densities of states is the appearance of a narrow band below the bottom of the bulk O $p$ bands of the ideal $PO_4$ groups. These narrow bands correspond to $2p\sigma$ states of the bridging O or N ion. Since these bridging ions are close to two P ions, it is not surprising that their local electrostatic potential energy is substantially lower than that of tetrahedrally coordinated ions which are close to only one P ion. In fact, the density-of-states plots in Fig. 5 show that states associated with the $O_3P$-N-$PO_3$ or $O_3P$-O-$PO_3$ defect are shifted to lower energy relative to the energies of states associated with the crystalline $PO_4$ groups. The density-of-states results also show that the bridging N states are generally higher in energy than the corresponding bridging O states, which is a reflection of the fact that the N nucleus ($Z=7$) binds its electrons less strongly than does the O nucleus ($Z=8$). As a consequence, the top valence state of the PNP material has a large contribution from the bridging N site, while the top valence state of the POP material is mainly due to the O bands of the $PO_4$ electrons.

The nature of these bridging N states is further illustrated in contour plots of the charge associated with the low-energy and high-energy valence states as shown in Fig. 6. From this figure, it is evident that the lower-energy state is well described by a bent N $2p\sigma$ molecular orbital, while the upper-energy state is well described by a N $2p\pi$ molecular orbital,
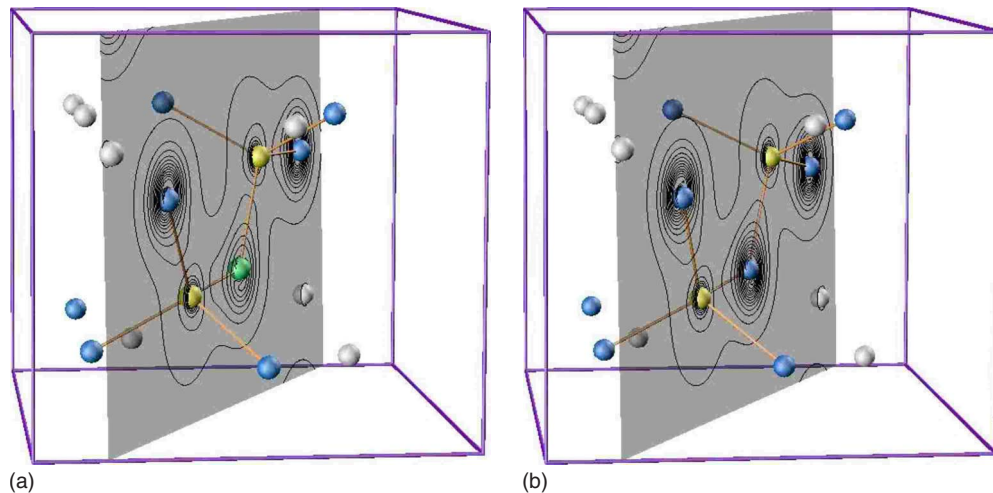


FIG. 3. (Color online) Bent (a) PNP and (b) POP defect structures shown with a ball-and-stick diagram within the section of the supercell indicated in Fig. 1. In addition, a contour plot of the valence electron density is plotted on the P-N-P and P-O-P planes. Contours are given in intervals of 0.2 $e/Å^3$, starting with the lowest contour at 0.2 $e/Å^3$.
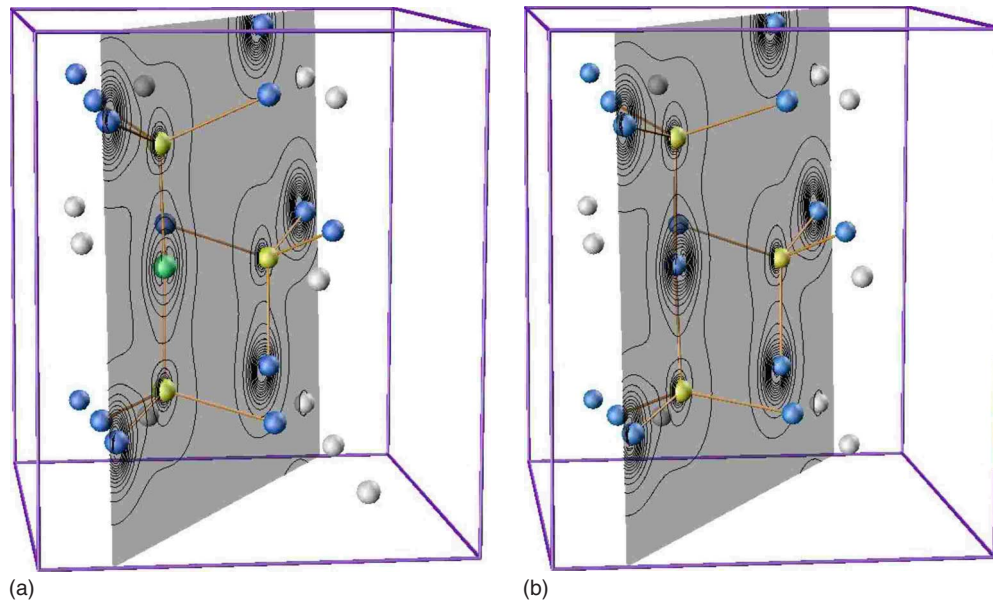
FIG. 4. (Color online) Straight (a) PNP and (b) POP defect structures shown with a ball-and-stick diagram within the section of the supercell indicated in Fig. 2. In addition, a contour plot of the valence electron density is plotted in the P-N-P and P-O-P planes using the same scale as in Fig. 3.

hybridized with $2p\pi$ molecular orbitals associated with nearby O ions.

The simulations find the isolated PNP and POP defects to be quite stable. Table I summarizes the structural parameters and relative energies found for the lowest-energy configura-
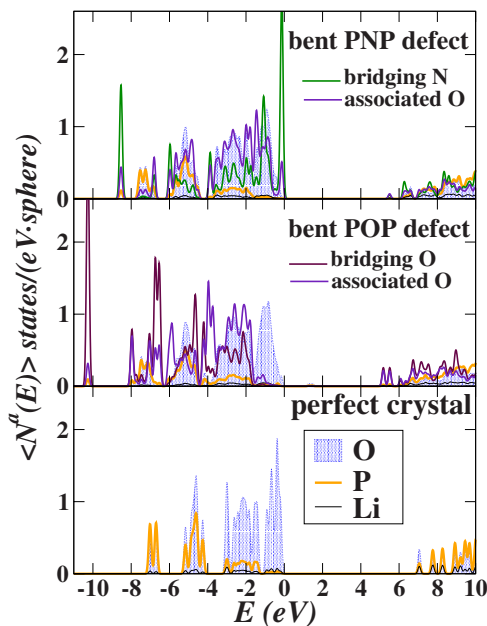


FIG. 5. (Color online) Plots of partial densities of states $\langle N^a(E) \rangle$ [as defined in Eq. 1 of Ref. 1], averaging over all spheres within the supercell for each type of site for bent PNP and POP defects compared with that of the ideal supercell of $\gamma$-Li$_3$PO$_4$. In the top two plots, partial densities of states for the bridging site and for the O sites bonded ("associated") with the PNP and POP defect are indicated separately. The zero of energy is fixed at the top of the highest occupied valence state.

tions of these defects, comparing results derived from the $\gamma$ and $\beta$ crystalline forms as computed using the Li$_{3-1/16}$PO$_{4-2/16}$N$_{1/16}$ supercells. Table I shows that the two P-O or P-N bonds in the defects are not quite equivalent. Having the length of 1.6 Å $\leq b \leq$ 1.7 Å, they are longer than the P-O bond length in PO$_4$, which is 1.5 Å. The bent structures have bond angles of $120° \leq \theta \leq 130°$, while the straight structures have bond angles of $160° \leq \theta \leq 180°$. For the $\gamma$ crystal phase, the bent PNP defect is more stable than the straight structure, while for the POP defect the straight structure is more stable than the bent one. Our simulations also indicate that in all of the rebonded phosphate structures studied, structures with N occupying the bridging site are more stable than those with N occupying a tetrahedral phosphate site by nearly 3 eV.[30] While the $\beta$ crystalline phase differs from the $\gamma$ phase by the orientations of the phosphate groups, very similar PNP and POP structures are formed as described in Table I. For the $\beta$ crystal phase, the straight PNP and POP structures are more stable than the corresponding bent structures.

The fact that the bridge-bonded groups exist in both bent and straight structures has been previously discussed in the literature. For example, quantum chemical calculations on H$_4$P$_2$O$_7$ molecules[32] found the structure to be optimized with a bridging bond angle of 131° with a very shallow minimum for the angular range of $120°-180°$.

With closer examination, it is evident that both the bent and straight defect structures are not small compared with the size of the simulation supercell. In order to quantify this problem for the $\gamma$ structure, in addition to the "$2c$" 128-atom supercell ($a \times 2b \times 2c$), we also performed a few calculations based on a $3c$ 192-atom supercell ($a \times 2b \times 3c$). While the stoichiometry of the $2c$ supercell was Li$_{3-1/16}$PO$_{4-2/16}$N$_{1/16}$, the $3c$ supercell was Li$_{3-1/24}$PO$_{4-2/24}$N$_{1/24}$. The corresponding lowest-energy configurations for the bent and straight

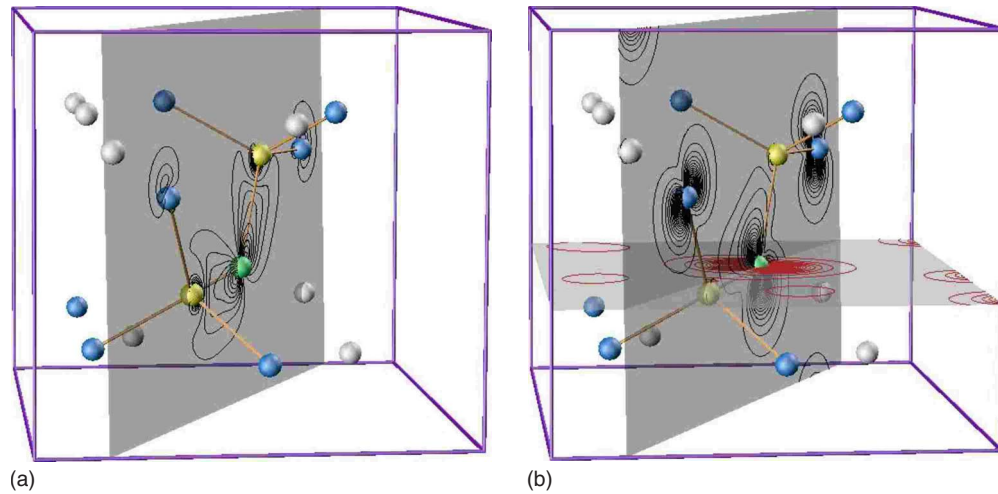(a)                                        (b)

FIG. 6. (Color online) Bent PNP defect structures shown with a ball-and-stick diagram within the section of the supercell indicated in Fig. 1, with contour plot of partial valence electron densities plotted on one or more planes. Contours are given in intervals of 0.1 $e/Å^3$, starting with the lowest contour at 0.05 $e/Å^3$. Diagram (a) corresponds to the low-energy states $-9.2$ eV $\leq E \leq -8.1$ eV, while diagram (b) corresponds to the states at the top of the band, $-1.6$ eV $\leq E \leq 0$ eV.

PNP structures in the $3c$ supercell are shown in Figs. 7 and 8, respectively. From these figures, we see that while the defect structures themselves are very similar in the two supercells, the ground-state Li-ion configuration is different for the straight PNP structure in the $3c$ supercell, where the most stable vacancy site is site 5.

In addition to studying the most stable configurations of the defects within our supercells, we are interested in the mobility of the Li ions, and have studied how the defect geometries and energies change when the Li-ion vacancy site changes. Using the site labels given in Figs. 1, 2, 7, and 8, the structural parameters and energies of the bent and

TABLE I. Summary of structural parameters for the most stable PNP and POP defects simulated in the $Li_{3-1/16}PO_{4-2/16}N_{1/16}$ supercells shown in Figs. 1 and 2 and similar supercells based on $\beta$-$Li_3PO_4$. Listed are the P-O or P-N bond lengths ($b$) in angstroms, P-N-P or P-O-P bond angles ($\theta$) in degrees, and relative supercell energies ($\Delta E$) in eV using the energy of the lowest-energy bent PNP defect derived from $\gamma$-$Li_3PO_4$ as the reference.

| Type | $b$ | $\theta$ | $\Delta E$ |
|---|---|---|---|
| | $\gamma$-$Li_3PO_4$ | | |
| P-N-P (bent) | 1.63, 1.67 | 118 | 0.00 |
| P-N-P (straight) | 1.63, 1.62 | 174 | 0.05[a] |
| P-O-P (bent) | 1.66, 1.69 | 123 | 2.71 |
| P-O-P (straight) | 1.69, 1.68 | 171 | 2.59 |
| | $\beta$-$Li_3PO_4$ | | |
| P-N-P (bent) | 1.64, 1.69 | 124 | 0.26 |
| P-N-P (straight) | 1.62, 1.64 | 168 | $-0.58$ |
| P-O-P (bent) | 1.66, 1.73 | 126 | 2.85 |
| P-O-P (straight) | 1.66, 1.72 | 164 | 2.38 |

[a]Simulations of these structures in the larger supercell ("$3c$") find the lowest-energy straight PNP defect to have an energy of 0.17 eV higher than that of the corresponding bent PNP defect.

straight PNP structures for different Li-ion vacancy sites are listed in Table II including results for both the $3c$ and $3c$ supercells. These results indicate that the PNP geometries are quite insensitive to the Li-ion vacancy positions, but the energy of the defect varies by nearly 1 eV with Li-ion vacancy position. For the bent PNP defect, the $2c$ supercell results are very similar to the $3c$ supercell results for Li-ion vacancy positions such as sites 1 and 5, which are close to the defect. But for Li-ion vacancy positions farther from the defect, the relaxation energies differ by more than 0.3 eV. For the straight PNP defect, the differences between the $2c$ and $3c$ are considerable. In fact, while in the $2c$ model, the lowest-energy Li-ion vacancy position is located on the equivalent sites 1 and 2, for the $3c$ model the configuration with the Li-ion vacancy on site 5 has an energy lower by 0.21 eV.
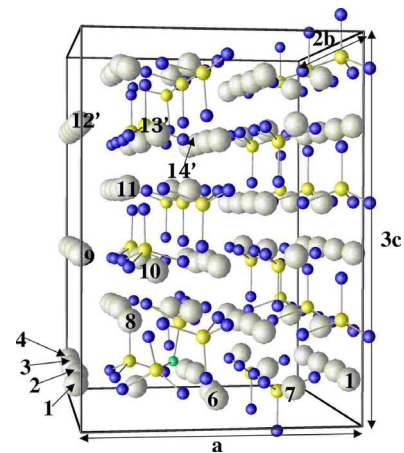


FIG. 7. (Color online) Ball-and stick-diagram of the lowest-energy configuration of the relaxed bent PNP structure in the $3c$ supercell corresponding to the similar structure shown in Fig. 1(b) for the $2c$ supercell. Labels on the Li sites correspond to those given in Fig. 1(a) with a few additional labels indicated with primes.
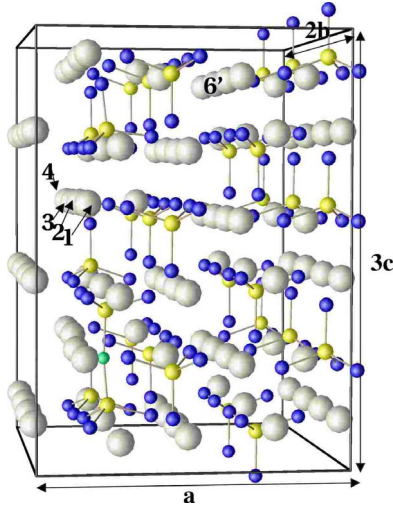
FIG. 8. (Color online) Ball-and-stick diagram of the lowest-energy configuration of the relaxed straight PNP structure in the $3c$ supercell corresponding to the similar structure shown in Fig. 2(b) for the $2c$ supercell, except that the $3c$ ground-state position of the Li-ion vacancy is at site 5 rather than at site 2. Labels on the Li sites correspond to those given in Fig. 2(a) with a few additional labels indicated with primes.

## B. Simulations of Li-ion vacancy migration

Having established in Sec. III A that oxygen vacancies in the form of POP and PNP defects embedded in $Li_3PO_4$ crystals stabilize Li-ion vacancies, the next question is, what is their effect on the mobility of Li-ion vacancies? Specifically, how does the mobility near the defect sites compare with the mobility in the bulk regions of the crystal? Since our simulation cells are relatively small, we have to be careful in interpreting our results. It is helpful to use the mobility simulations for bulk crystals studied in our earlier work[1] for comparison. In order to facilitate this comparison, we have shifted our energy references to coincide with the corresponding bulk sites. Because of the crystal symmetry, there are two inequivalent Li sites in the bulk lattice and correspondingly, two metastable Li-ion vacancy sites with an energy of 0.00 eV corresponding to sites 5, 7, and 10 in Fig. 1(a) and site 5 in Fig. 2(a) and with an energy of 0.20 eV corresponding to sites 1–4, 6, 8, and 9 in Fig. 1(a) and sites 1–4 in Fig. 2(a). In the present work, we studied a few representative migration paths using our supercells representing PNP and POP defects in $\gamma$-$Li_3PO_4$. We find that the migration barriers for hops between adjacent metastable sites fall into three categories—$E_m^{near}$, $E_m^{trans}$, and $E_m^{tot}$. $E_m^{near}$ represents steps in the vicinity of the defect. $E_m^{tot}$ represents the total or overall migration barrier for a vacancy to move from a site

TABLE II. Summary of structural parameters for the PNP defects simulated in the $2c$ and $3c$ supercells for various Li-ion vacancy positions identified in Figs. 1, 2, 7, and 8. The notation and units are the same as those used in Table I. The energy references for the relative energies $\Delta E$ are taken separately for the bent and straight PNP structures and are taken separately for the $2c$ and $3c$ simulation cells as indicated by the corresponding "0.00" entries in the $\Delta E$ column.

| Position | $b$ | | $\theta$ | | $\Delta E$ | |
|---|---|---|---|---|---|---|
| | $2c$ | $3c$ | $2c$ | $3c$ | $2c$ | $3c$ |
| | | Bent P-N-P | | | | |
| 1 | 1.63, 1.67 | 1.63, 1.67 | 117 | 117 | 0.04 | 0.06 |
| 2 | 1.63, 1.68 | | 118 | | 0.83 | |
| 3 | 1.63, 1.66 | | 119 | | 0.84 | |
| 4 | 1.63, 1.67 | | 117 | | 0.78 | |
| 5 | 1.63, 1.67 | 1.63, 1.67 | 118 | 117 | 0.00 | 0.00 |
| 6 | 1.62, 1.68 | | 118 | | 0.75 | |
| 8 | 1.64, 1.69 | 1.64, 1.68 | 113 | 113 | 0.34 | 0.52 |
| 9 | 1.63, 1.67 | 1.63, 1.66 | 117 | 118 | 0.52 | 0.85 |
| 10 | 1.63, 1.67 | 1.63, 1.66 | 117 | 118 | 0.36 | 0.59 |
| 11 | | 1.63, 1.66 | | 118 | | 0.79 |
| 12' | | 1.63, 1.67 | | 118 | | 0.52 |
| 13' | | 1.63, 1.67 | | 117 | | 0.46 |
| 14' | | 1.63, 1.66 | | 118 | | 0.87 |
| | | Straight P-N-P | | | | |
| 1 and 2[a] | 1.62, 1.63 | 1.62, 1.64 | 174 | 176 | 0.00 | 0.21 |
| 3 and 4[a] | 1.62, 1.64 | | 180 | | 1.15 | |
| 5 | 1.61, 1.64 | 1.61, 1.64 | 170 | 173 | 0.02 | 0.00 |
| 6' | | 1.61, 1.65 | | 179 | | 1.18 |

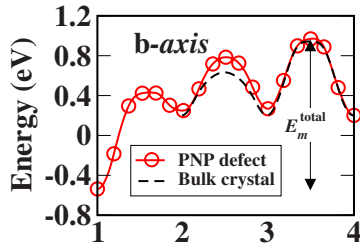[a]These sites are related by symmetry.

FIG. 9. (Color online) Energy path for Li-ion vacancy hopping between sites indicated in Fig. 1(a) along the **b** axis of the bent PNP $2c$ supercell. Symbols represent NEB images, while the solid curve is a smooth interpolation between the calculated results. For comparison, the energy path for the bulk crystal is indicated with the dashed black line. The energies calculated for the defect and bulk structures were shifted to coincide at vacancy configuration 4.

close to the defect to the bulk region of the crystal. Because of our supercell sizes, not all of the simulated migration paths can estimate this number. $E_m^{trans}$ represents an intermediate or transition migration energy barrier. The results for these energies determined in our simulations are summarized and discussed in Sec. VI below. Particular examples of vacancy diffusion processes are detailed below.

First, consider vacancy diffusion along the **b** axis near the bent PNP structure shown in Fig. 1, hopping between sites $1 \leftrightarrow 2 \leftrightarrow 3 \leftrightarrow 4$. In this case, the vacancy at site 1 is close to the O vacancy site but site 2 is farther away, having an energy of $\Delta E = 0.8$ eV higher and the corresponding "transition" migration energy is $E_m^{trans} = 1.0$ eV. In this case, site 4 is reasonably far from the defect site so that we can get a good estimate for the total migration barrier for this process of $E_m^{tot} = 1.5$ eV. The corresponding energy-path diagram shown in Fig. 9 has been adjusted so that the energy at site 4 coincides with the bulk value of 0.2 eV reported in our previous work.[1] From this figure, it is evident that the PNP defect provides a trap of $-0.5$ eV compared to the lowest-energy vacancy site in the bulk crystal.

A second example is presented in Fig. 10, where vacancy diffusion along the **a** axis is plotted near the bent PNP and POP structures with the metastable vacancy sites at $1 \leftrightarrow 5 \leftrightarrow 6 \leftrightarrow 7 \leftrightarrow 1$. The figure illustrates the similarity of the energy landscapes for vacancy diffusion near the PNP and POP structures. From this comparison, we estimate that the
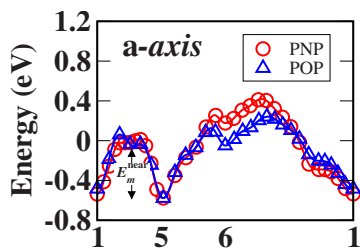


FIG. 10. (Color online) Energy path for Li-ion vacancy hopping between sites indicated in Fig. 1(a) along the $a$ axis of the bent PNP $2c$ supercell using the same notation and energy shift as in Fig. 9. For comparison, the corresponding energy path for the bent POP structure is plotted in the same graph, with energies set to coincide at site 5.
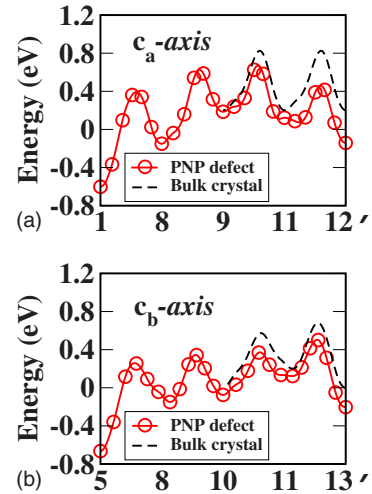


FIG. 11. (Color online) Energy path for Li-ion vacancy hopping between sites indicated in Fig. 7 along the **c** axis of the bent PNP $3c$ supercell. For comparison, the corresponding energy path for the bulk crystal is indicated with the dashed line. The energy scale of the plots was adjusted so that the energy of a vacancy at site $14'$ in this supercell coincides with the bulk value of 0.2 eV reported in our previous work (Ref. 1).

bridging atom (O or N) affects the Li-ion migration energies by no more than 0.2 eV. In this case, the step $1 \leftrightarrow 5$ involves sites very near the O vacancy and $E_m^{near} = 0.6$ eV is found for both the PNP and POP defects. This is slightly smaller than the corresponding migration energy in the bulk material.[1] However, diffusion further away from the defect in our simulations is complicated by supercell effects. In fact, because of the strong repulsion of the O vacancy site, the Li-ion vacancy is actually unstable at site 7 in this supercell. Evidence of the strong repulsion of the O vacancy to Li ions can be seen in Figs. 1(b) and 7, where the equilibrium position of Li ion at site 1 is pushed away from the vicinity of the O vacancy. We estimate $E_m^{trans}$ to be 0.8 eV, but the complete path in this supercell cannot estimate the overall migration energy $E_m^{tot}$ along the **a** axis for an isolated defect of this type.

In Fig. 11, two vacancy diffusion paths are shown along the **c** axis of the crystal. The simulations were performed using the larger $3c$ supercell and the energy scale was adjusted so that the energy of a vacancy at site $14'$ in this supercell coincides with the bulk value of 0.2 eV reported in our previous work.[1] In this case, the vacancy near the PNP defect is trapped by an energy of between $-0.6$ and $-0.7$ eV compared to the lowest-energy vacancy site of the bulk crystal. The overall migration energy for diffusion along the **c** axis into the bulk region is $E_m^{tot} \approx 1.2 - 1.3$ eV.

As a final example of the vacancy diffusion analysis, we show **b**-axis diffusion near the oxygen vacancy in the straight PNP structure in Fig. 12. In this case, the hopping step $1 \leftrightarrow 2$ takes place very near to the O vacancy and the energy is consequently small. We find $E_m^{near} = 0.5$ or 0.4 eV for the $2c$ or $3c$ supercells, respectively. In contrast to the **b**-axis diffusion near the bent PNP shown in Fig. 9, the hopping step $2 \leftrightarrow 3$ is still close to the defect region and even step $3 \leftrightarrow 4$ is not well converged to the bulklike values.

The general conclusion that can be drawn from this migration-path studies is that Li-ion vacancy hopping steps
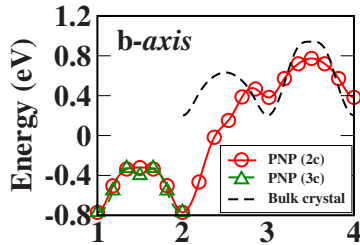
FIG. 12. (Color online) Energy path for Li-ion vacancy hopping between sites indicated in Figs. 2(a) and 8 along the **b** axis of the straight PNP defect, comparing results for the $2c$ and $3c$ supercells. The corresponding energy path for the bulk crystal is indicated with the dashed line. The energy scale of the plots was adjusted so that the energy of a vacancy at site $6'$ in the $3c$ supercell coincides with the bulk value of 0.2 eV reported in our previous work (Ref. 1) and the two energy-path diagrams were set to coincide at site 1.

near the defects have migration energies comparable or smaller than the corresponding energies in the bulk materials, but the overall migration energy for the vacancy to escape from an isolated PNP or POP defect into the bulk region of the crystal can be as high as 1.5 eV. The actual migration energies of crystals with a finite concentration of PNP or POP defects would depend very strongly on the concentration as perhaps can be estimated from the $E_m^{\text{trans}}$ values of our simulations.

## IV. PO$_3$N DEFECTS ASSOCIATED WITH INTERSTITIAL Li IONS

In our previous work,[1] we found metastable interstitial sites for Li ions in **c**-axis channels in $\gamma$-Li$_3$PO$_4$, the most stable of which we labeled "$I_0$." One method of stabilizing extrinsic interstitial Li ions at the $I_0$ site is to replace an O with a N in a phosphate group, forming a PO$_3$N defect. Figure 13 shows the relaxed geometry of the most stable of these configurations for an interstitial Li ion at site $I_0^1$.[33] The structural parameters are summarized in Table III. For com-
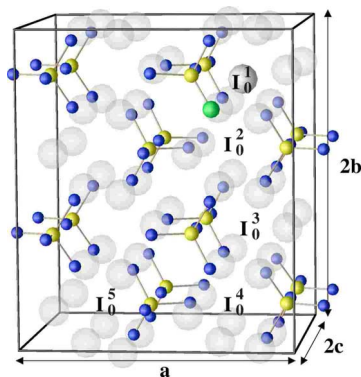
TABLE III. Summary of energies and structural parameters of metastable interstitial Li-ion sites in the N-doped $\gamma$-Li$_3$PO$_4$ supercell shown in Fig. 13. For each configuration, the lengths of the P-N bond and the three P-O bonds for the PO$_3$N defect are listed in angstroms. Also listed is the energy ($\Delta E$ in eV) of each configuration relative to that of the bulklike site $I_0^5$.

| Li-ion site | P-N | P-O | $\Delta E$ |
|---|---|---|---|
| $I_0^1$ | 1.56 | 1.58, 1.58, 1.61 | −0.58 |
| $I_0^2$ | 1.57 | 1.58, 1.58, 1.59 | −0.57 |
| $I_0^3$ | 1.56 | 1.58, 1.58, 1.59 | 0.06 |
| $I_0^4$ | 1.55 | 1.58, 1.58, 1.60 | −0.05 |
| $I_0^5$ | 1.55 | 1.58, 1.58, 1.59 | 0.00 |

parison, the P-O bond lengths in $\gamma$-Li$_3$PO$_4$ are 1.54–1.55 Å. We note that the P-N bond is very slightly larger ($\approx 1.56$ Å) and the three P-O bonds are even larger ($\approx 1.59$ Å) in the PO$_3$N defect. From the table, it is apparent that P-N and P-O bond lengths are insensitive to the site of the interstitial Li ion, although the metastable energies range from −0.6 eV (for $I_0^1$ and $I_0^2$ near the N site) to 0.0 eV (for $I_0^5$ assumed to well approximate the bulk crystal interstitial environment).

The partial densities of states for the ground-state $I_0^1$ configuration are shown in Fig. 14, illustrating that the states associated with the N site are at higher energy than the O states of the PO$_4$ groups. This is presumably due to the smaller binding energy of the N nucleus compared to that of the O nucleus. Interestingly, the contributions from the associated (PO$_3$N) O states are also shifted to higher energies than those of the O states of the PO$_4$ groups. The highest-energy occupied states are mainly localized on the N site and have $2p\pi$ character, separated by 1.5 eV above the top of the bulk valence band. While the simulation material is still a very good insulator, the extent to which the distribution of band energies contributes to the binding energy of the material suggests that the PO$_3$N groups would tend to be less stable than the PO$_4$ groups. More details of these states are presented in the supplemental materials for this paper.[31]

Having established that the PO$_3$N defect can stabilize interstitial Li ions, we also studied their effects on the migration of interstitial Li ions. In our studies of interstitial Li-ion migration in bulk Li$_3$PO$_4$,[1,2] we found that an interstitialcy mechanism, involving the concerted motion of an interstitial Li ion and a neighboring Li ion of the host lattice, was en-



FIG. 13. (Color online) Ball-and-stick diagram of the lowest-energy configuration ($I_0^1$) of the $\gamma$-Li$_3$PO$_4$ supercell with a N ion substituting for an O ion and a metastable Li ion at a nearby interstitial site, using the same color conventions as in Fig. 1. The site labels $I_0^2, I_0^3, \ldots$ indicate other metastable interstitial sites used in the simulations.
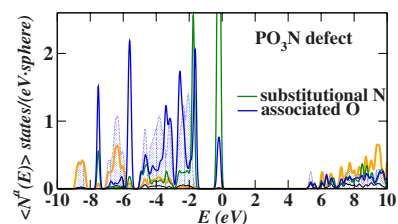


FIG. 14. (Color online) Plot of partial densities of states for substitutional N and interstitial Li ion corresponding to structure of the $I_0^1$ configuration shown in Fig. 13 using the same notation and conventions as in Fig. 5.
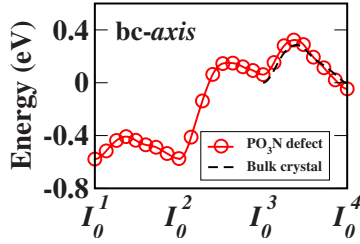
FIG. 15. (Color online) Energy-path diagram for interstitial Li-ion hopping via an interstitialcy mechanism between metastable $I_0$ sites indicated in the N-doped supercell shown in Fig. 13. The zero of energy was taken to be at site $I_0^5$ of the structural diagram. For comparison, the corresponding energy path of the bulk $\gamma$-Li$_3$PO$_4$ supercell (Ref. 1) is indicated with a dashed black line.

ergetically favorable (by more than 1 eV) compared to a direct hopping mechanism. Therefore, the interstitial ion migration in this work focused on the interstitialcy mechanism. The energy path for migration along the **b** and **c** axes, between the $I_0^1 \leftrightarrow I_0^2 \leftrightarrow I_0^3 \leftrightarrow I_0^4$ sites, is shown in Fig. 15 and the results are summarized in Sec. VI. Among the several interstitialcy paths investigated, the path shown in Fig. 15 shows the representative features. For the first step, $I_0^1 \leftrightarrow I_0^2$, both the initial interstitial Li ion at site $I_0^1$ and the host Li ion which moves to site $I_0^2$ neighbor the N site. The resulting energy barrier $E_m^{near}$ for this step is the smallest barrier found in these simulations. While the lowest-energy $I_0^1$ configuration is "trapped" by the PO$_3$N defect by approximately −0.6 eV compared to the corresponding $I_0^5$ configuration which approximates the bulk environment, the motion of the Li ion between the sites $I_0^1 \rightarrow I_0^2$ is characterized by a very small migration energy of $E_m^{near}=0.2$ eV. We estimate the total migration energy for the interstitial ion to escape from the $I_0^1$ configuration to the bulk region to be $E_m^{tot}=0.9$ eV. In an electrolyte material with an appreciable concentration of PO$_3$N defects, we would expect the total migration energy of an interstitial Li ion to be approximated by the transition energy barrier of $E_m^{trans}=0.7$ eV.
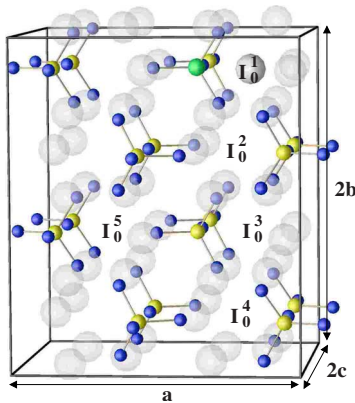


FIG. 16. (Color online) Ball-and-stick diagram of the lowest-energy configuration ($I_0^1$) of the $\gamma$-Li$_3$PO$_4$ supercell with a Si ion substituting for a P ion and a metastable Li ion at a nearby interstitial site, using the same color conventions as in Fig. 1 except that the Si is indicated with a green ball. The site labels $I_0^2, I_0^3, \ldots$ indicate other metastable interstitial sites used in the simulations.

TABLE IV. Summary of energies and structural parameters of metastable interstitial Li-ion sites in the Si-doped $\gamma$-Li$_3$PO$_4$ supercell shown in Fig. 16. For each site, the Si-O bond lengths are given in angstroms and the relative energy $\Delta E$ is given in eV with the bulk-like site $I_0^5$ chosen as the reference energy.

| Site | Si-O | $\Delta E$ |
|---|---|---|
| $I_0^1$ | 1.62, 1.66, 1.66, 1.62 | −0.51 |
| $I_0^2$ | 1.63, 1.63, 1.67, 1.62 | −0.35 |
| $I_0^3$ | 1.63, 1.64, 1.64, 1.63 | 0.04 |
| $I_0^4$ | 1.63, 1.64, 1.63, 1.63 | −0.09 |
| $I_0^5$ | 1.63, 1.64, 1.64, 1.63 | 0.00 |

## V. SiO$_4$ DEFECTS ASSOCIATED WITH INTERSTITIAL Li IONS

Another method of stabilizing extrinsic interstitial Li ions is to substitute Si for P. A supercell constructed to study this situation is shown in Fig. 16 corresponding to the stoichiometry of Li$_{3+1/16}$Si$_{1/16}$P$_{1-1/16}$O$_4$.

The structural parameters of the relaxed SiO$_4$ defect are given in Table IV. The Si-O bond lengths are 1.62–1.67 Å, which are very similar to bond lengths in crystalline SiO$_2$ materials such as quartz,[34] but larger than the 1.54–1.55 Å P-O bond lengths in PO$_4$. As in the case of the interstitial Li ions stabilized by the PO$_3$N defect described in Sec. IV, the Si-O bond lengths are very insensitive to the interstitial Li-ion position. In this case, the metastable energy of interstitial Li ion at the most stable configuration ($I_0^1$) is −0.5 eV relative to the bulklike configuration ($I_0^5$) set at 0.0 eV.

Figure 17 shows the partial densities of states for the ground-state $I_0^1$ configuration of the SiO$_4$ defect. The Si states are at slightly higher energy than the corresponding P states and the O contributions associated with the SiO$_4$ defect lie at slightly higher energy than the O contributions from the PO$_4$ group. The partial-density-of-states profile for this case is very similar to that of the bulk $\gamma$-Li$_3$PO$_4$ material, suggesting that the SiO$_4$ defect is relatively stable.

We also studied the migration of the interstitial Li ion in the presence of the SiO$_4$ defect, finding results remarkably similar to those of the PO$_3$N defect. The corresponding energy-path diagram is shown in Fig. 18 and the migration energy results are summarized in Sec. VI. Specifically for the SiO$_4$ defect, the trapping energy of the interstitial Li ion at the lowest-energy $I_0^1$ configuration is approximately −0.5 eV
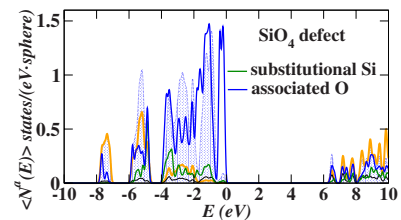


FIG. 17. (Color online) Plots of partial densities of states for substitutional Si and interstitial Li corresponding to structure of the $I_0^1$ configuration shown in Fig. 16 using the same notation and conventions as in Fig. 5.
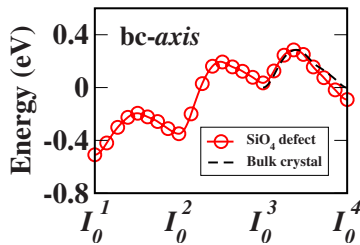
FIG. 18. (Color online) Energy-path diagram for interstitial Li-ion hopping via an interstitialcy mechanism between metastable $I_0$ sites indicated in the Si-doped supercell shown in Fig. 16. The zero of energy was taken to be at site $I_0^5$ of the structural diagram. For comparison, the corresponding energy path of the bulk $\gamma$-Li$_3$PO$_4$ supercell (Ref. 1) is indicated with a dashed black line.

compared to the corresponding bulklike $I_0^5$ configuration and the migration energies of the interstitial Li ions are determined to be $E_m^{near} = 0.3$ eV and $E_m^{tot} = 0.8$ eV.

## VI. COMPARISON WITH EXPERIMENT

In Secs. III and V, we have studied the energetics and migration properties of the extrinsic mobile Li ions in supercells of Li$_3$PO$_4$. Fortunately, many experimental studies on related materials are connected with these simulations.

### A. Structures and energies of isolated defects in Li$_3$PO$_4$ crystals

In Sec. III A, we discussed the formation of stable rebonded phosphate structures PNP and POP within the Li$_3$PO$_4$ simulation cells. In fact, similar structures have been directly identified in polycrystalline phosphate materials[7] and have also been identified in glass phosphate materials using spectroscopic tools.[6] Several examples of bridging PNP and POP structures in crystalline materials are summarized in Table V. For example, PON has several structural forms[34] which can be described in terms of tetrahedra of PO$_2$N$_2$ connected through shared O or N ions located at the tetrahedral corners which correspond to the bridging -N- or -O- ions in our terminology. The authors of Ref. 34 stated that this bridging bond is very flexible so that the material has several crystalline and disordered phases. As discussed in Sec. III A, a low-energy $2p\sigma$ bond of the bridging N or O, hybridizing with the P 3$s$ states, contributes to the stability of the bridging bond. The fact that the energy of these low-lying states is determined by the strong electrostatic field of the P ions and that the hybridization can occur in both bent and straight PNP and POP structures is consistent with the notion that the bonds are flexible. These flexible bridging bonds are also present in phosphorus oxide,[35,36] P$_2$O$_5$, and in the lithium phosphite and diphosphate materials,[37,38] LiPO$_3$ and Li$_4$P$_2$O$_7$, and has also been studied with quantum chemical techniques in hydrogen phosphate clusters,[32] H$_4$P$_2$O$_7$. In the crystalline materials listed in Table V, the bridging bond lengths vary between 1.56 and 1.63 Å, increasing with increasing Li-ion concentration. The bridging bond lengths reported for our simulations on Li$_{3-z}$PO$_{4-2z}$N$_z$ as listed in Tables I and II are slightly larger than those listed in Table V. For those simulations, the bridging bond angles were ap-

TABLE V. Bridging PNP and POP bond lengths ($b$ in Å) and angles ($\theta$ in degrees) found in crystalline materials.

| Material | Structure | Reference | $b$ | $\theta$ |
|---|---|---|---|---|
| P$_2$O$_5$ | $Pnma$ | 35 | 1.57 | 144 |
| P$_2$O$_5$ | $Fdd2$ | 36 | 1.56–1.58 | 123–136 |
| PON | $P3_221$ | 34 | 1.57–1.58 | 141 |
| PON | $I\bar{4}2d$ | 34 | 1.58 | 132 |
| LiPO$_3$ | $Pn$ | 37 | 1.57–1.63 | 127–140 |
| Li$_4$P$_2$O$_7$ | $P\bar{1}$ | 38 | 1.62–1.63 | 137 |

proximately 120° or 170°–180° for bent and straight PNP and POP structures. For the crystalline materials listed in Table V, the bond angles are 120°–140°. Since the isolated bridging bond is so flexible, it is probable that the bridging bond angle found in each material is primarily determined by spatial constraints and optimization of the packing volumes.

Wang *et al.*[7] were able to make a doped polycrystalline material with the stoichiometry of Li$_{2.88}$PO$_{3.73}$N$_{0.14}$. Using chemical and spectral analysis, they identified PO$_3$N and PNP groups. Evidence of PNP and POP structures within glassy phosphorus oxynitride materials has been inferred from various experimental probes.[6,39] Cross-linked PNP and POP chains are thought to be responsible for the chemical and thermal stability of LiPON thin films. Our simulations of the PNP and POP structures clearly indicate that N prefers the bridging PNP configuration relative to the tetrahedral PO$_3$N configuration by nearly 3 eV. However, in the pure PON structures[34] the N preference for the bridging site is apparently not observed. Spectroscopic evidence in phosphorus oxynitride glasses[39,40] suggests that N is found in both bridging and tetrahedral sites in these materials.

For the case of Si substituting for P to make a SiO$_4$ defect, there has been considerable experimental study. In 1977, Hu *et al.*[9] studied the lithium-ion conductivity in solid solutions of Li$_4$SiO$_4$ and Li$_3$PO$_4$. The crystal structure of Li$_4$SiO$_4$ has several different forms,[41–43] corresponding to slightly different arrangements of the tetrahedral SiO$_4$ groups and the Li ions. In the solid solution of Li$_4$SiO$_4$ and Li$_3$PO$_4$, Baur and Ohta[10] noted that there is a discontinuity in the lattice constants at a 50% mixture, suggesting that P↔Si substitution can occur within similar crystal structures in the two concentration ranges of $0 \le u \le 0.5$ and $0.5 \le u \le 1$ corresponding to Li$_{3+u}$Si$_u$P$_{1-u}$O$_4$. The range $0 \le u \le 0.5$ with the Li$_3$PO$_4$-like structures is most directly related to the simulations in the present work. There has been at least one study[11] that investigated these materials as electrolytes in battery conditions which found the Li$_3$PO$_4$/Li$_4$SiO$_4$ solid solution to be stable with respect to Li metal as well as with respect to the cathode material for at least for 3 weeks. However, earlier work by the Oak Ridge group[4] found that glassy electrolyte films made from $x$Li$_2$O·$y$SiO$_2$·$z$P$_2$O$_5$ composites in contact with lithium-metal anodes decompose after a few weeks. On the other hand, lithium silicates based on quartzlike structures with edge-sharing SiO$_4$ tetrahedra[44,45] seem to form pockets of Li-Si alloys during electrochemical processing in the presence of Li metal.

TABLE VI. Summary of results for Li-ion migration energies $E_m^{\text{near}}$, $E_m^{\text{trans}}$, and $E_m^{\text{tot}}$ in eV. The migration energies of Li-ion vacancies via a direct hopping mechanism summarize results presented in Sec. III B. The migration energies of interstitial Li ions via an interstitialcy mechanism summarize results presented in Secs. IV and V. The "Cell" column refers to the smaller (2c) and larger (3c) simulation cells.

| Type | Defect | Axis | Cell | $E_m^{\text{near}}$ | $E_m^{\text{trans}}$ | $E_m^{\text{tot}}$ |
|------|--------|------|------|------|------|------|
| Vacancy | Bent PNP | **a** | 2c | 0.6 | 0.8 | |
| Vacancy | Bent POP | **a** | 2c | 0.6 | 0.7 | |
| Vacancy | Bent PNP | **b** | 2c | | 1.0 | 1.5 |
| Vacancy | Bent PNP | **c**$_a$ | 3c | | 1.0 | 1.3 |
| Vacancy | Bent PNP | **c**$_b$ | 3c | | 0.9 | 1.2 |
| Vacancy | Straight PNP | **b** | 2c | 0.5 | 1.2 | |
| Vacancy | Straight PNP | **b** | 3c | 0.4 | | |
| Interstitial | PO$_3$N | **bc** | 2c | 0.2 | 0.7 | 0.9 |
| Interstitial | SiO$_4$ | **bc** | 2c | 0.3 | 0.7 | 0.8 |

### B. Migration energies of mobile Li ions

As mentioned in Sec. III B, we found it useful to distinguish three types of migration steps–$E_m^{\text{near}}$, $E_m^{\text{trans}}$, and $E_m^{\text{total}}$. Table VI summarizes the results for all of the diffusion paths studied. The results show that energy barriers for the direct hopping of a Li-ion vacancy near a vacancy-related defect can be as small as $E_m^{\text{near}}=0.6$ eV, while energy barriers for interstitialcy migration of an interstitial Li ion near an interstitial-related defect can be as small as $E_m^{\text{near}}=0.2$ eV. On the other hand, the defects which stabilize the mobile Li ions also trap them so that the overall migration barriers for escaping from isolated defects can be as large as $E_m^{\text{total}}=1.5$ eV or $E_m^{\text{total}}=0.9$ eV for the vacancy or interstitial cases, respectively. On the other hand, for appreciable concentrations of defects, the transition migration energies shown in Table VI may be a more appropriate measure. From this table, it is evident that as in bulk Li$_3$PO$_4$, the migration of interstitial Li ions via the interstitialcy mechanism has a substantially lower migration energy than does the migration of Li-ion vacancies.

The experiments of Wang et al.[7] on the polycrystalline Li$_{2.88}$PO$_{3.73}$N$_{0.14}$ material, which measured an ionic activation energy of $E_A=0.97$ eV, relate most directly to our simulations on defects which stabilize Li-ion vacancies. In fact, the experimental defect concentration, corresponding to $x=-0.12$, $y=0.27$, and $z=0.14$, is somewhat larger than considered in our simulations with the smaller (2c) supercell with $-x=z=0.0625$ and $y=0.125$. If one argues that the experiment is characterized by a temperature-independent concentration of vacancies and that the intermediate migration energy of our simulations is likely to best approximate the experimental migration barriers, then our result of 0.7 eV $\leq E_m^{\text{trans}} \leq 1.0$ eV for the Li-ion vacancy migration near the bent PNP and POP structures is in good agreement.

Of technological interest is the higher-conductivity materials such as found in the LiPON films,[4,5,7,8,46–51] which have a wide range of stoichiometries with the smallest activation energies measured to be $E_A > 0.5$ eV.[52] The majority of the reported films have $x < 0$ corresponding to Li-ion vacancies. However, in these disordered structures, it is not really possible to classify the mobile ions in terms of vacancy or interstitial mechanisms. While the simulations that we have performed in this study do not directly relate to the glassy materials, we expect that the mobility of the ions near the isolated defect structures of our supercells may approximate some of diffusion steps found in the glassy materials. Further investigation of these systems is needed, especially to consider the effects on Li-ion migration due to extended defect geometries and disorder.

The experiments of Hu et al.[9] on Li$_{3+u}$Si$_u$P$_{1-u}$O$_4$ materials relate most directly to our studies of interstitial Li-ion diffusion described in Sec. V. The experiments[9] found the highest conductivity with an activation energy of $E_A=0.51$ eV at a mixture corresponding to the stoichiometry of Li$_{3.4}$Si$_{0.4}$P$_{0.6}$O$_4$, substantially lower than the activation energies of 0.87 and 1.30 eV for the pure Li$_4$SiO$_4$ and Li$_3$PO$_4$ materials, respectively. For the stoichiometry of Li$_{3.06}$Si$_{0.06}$P$_{0.94}$O$_4$, the authors found $E_A=0.60$ eV, which is not inconsistent with our supercell calculation results of $E_m^{\text{total}}=0.8$ eV for Li$_{3.0625}$Si$_{0.0625}$P$_{0.9375}$O$_4$. In general, our studies point to the conclusion that interstitial diffusion via an interstitialcy mechanism is energetically favorable compared with vacancy diffusion via a direct hopping mechanism in these systems. The solid-solution results of Li$_{3+u}$Si$_u$P$_{1-u}$O$_4$ for $0 \leq u \leq 0.5$ are likely to be an experimental realization of this mechanism. The fact that activation energy for this system is found to be as low as $E_A=0.51$ eV reinforces our conclusion.

Our results for the PO$_3$N defect system described in Sec. IV are very similar to those of the SiO$_4$. The experimental evidence for this case, however, is not as clear-cut since the incorporation of N into the Li$_3$PO$_4$ lattice at the tetrahedral PO$_3$N sites must compete with the formation of PNP structures. Interestingly, the results of conductivity measurements on Li$_{3+x}$PO$_{4-y}$N$_z$ films reported in the literature[5] find $E_m < 0.6$ eV for the largest values of $x$. On the other hand, these values of $E_m$ are not significantly smaller than those found in films with a significant amount of PNP and POP chains.[6]

### VII. SUMMARY AND CONCLUSIONS

The simulations in the Li$_3$PO$_4$ supercells have resulted in a number of interesting findings about the defect structures

and associated extrinsic mobile Li ions of this solid-state electrolyte material. We found that O vacancies form very stable POP defects involving the rebonding of two neighboring $PO_4$ groups. In the presence of nitrogen, the system can lower its energy by approximately 3 eV by replacing the bridging -O- with -N- compared to the N occupying a tetrahedral site ($PO_3N$). For the $\gamma$ and $\beta$ crystalline forms of $Li_3PO_4$, both bent and straight PNP and POP could be stabilized where the bridging bond angles were $120°-130°$ and $160°-180°$, respectively. The densities of states of these materials are characterized by a narrow band of states corresponding to $2p\sigma$ bonds of the bridging O or N which appears 1 eV or more below the valence states of $Li_3PO_4$ and undoubtedly contributes to the stability of the structures. These PNP and POP structural forms could be correlated with other crystalline phosphate materials where the structures are often described in terms of $PO_4$ tetrahedra where bridging bonds correspond to corner-sharing tetrahedra. It is also apparent that the POP and PNP defects are prototypes for more extended chains of bridging structures that have been studied in LiPON materials.[6] As defect structures in $Li_3PO_4$ crystals, both PNP and POP stabilize extrinsic Li-ion vacancies. We also found that it is possible to stabilize extrinsic interstitial Li ions by doping $Li_3PO_4$ crystals, substituting N for O or substituting Si for P to form $PO_3N$ or $SiO_4$ defects, respectively. Both of these defect structures involve minor changes to the host lattice. The $SiO_4$ defect could be correlated with experimental studies of solid solutions of $Li_3PO_4$ and $Li_4SiO_4$.[9]

In addition to stabilizing extrinsic mobile Li ions, the defect structures also tend to trap the vacancies or interstitial ions. By defining migration barriers for hops of the mobile Li ions between adjacent metastable sites in terms of three categories—$E_m^{near}$, $E_m^{trans}$, and $E_m^{tot}$—we are able to better analyze the results. $E_m^{near}$ represents diffusion steps of the vacancy or interstitial ion in the vicinity of the defect. $E_m^{tot}$ represents the total or overall migration barrier for the vacancy or interstitial ion to move from a site close to the defect to the bulk region of the crystal, while $E_m^{trans}$ represents an intermediate or transition migration energy. For the cases modeled in this study, we find that $E_m^{near}$ is less than or equal to the corresponding migration barrier in the bulk material, while $E_m^{trans}$ and $E_m^{tot}$ tend to be larger than the corresponding bulk values.

The migration-path analysis could be related most specifically to two experiments. For the case of the PNP defect, the experiments of Wang *et al.*[7] on polycrystalline $Li_{2.88}PO_{3.73}N_{0.14}$ material found a migration energy of $E_m$ =0.97 eV, which relates to our results of $0.7$ eV $\leq E_m^{trans} \leq 1.0$ eV for the Li-ion vacancy migration near bent PNP and POP structures. For the case of the $SiO_4$ defect, the experiments of Hu *et al.*[9] on solid solutions of $Li_3PO_4$ and $Li_4SiO_4$ that measured an ionic migration energy of $E_m$ =0.6 eV for 6% $Li_4SiO_4$ relate to our results of $E_m^{tot}$ =0.8 eV for interstitial Li-ion migration via an interstitialcy mechanism.

As in the bulk material, the interstitial Li-ion diffusion via the interstitialcy mechanism is energetically favorable compared to vacancy diffusion by direct hopping. Our results suggest that the interstitialcy mechanism is the dominant mechanism of Li-ion migration in $Li_{3+u}Si_uP_{1-u}O_4$ materials with $0 \leq u \leq 0.5$. It could also be the diffusion mechanism for materials with $PO_3N$ defects, which behave in a very similar way according to our calculations. However, in this case, further work is needed to understand the likelihood of forming the $PO_3N$ defects, which must compete with the formation of POP and PNP defects in the actual material.

The LiPON materials are disordered, but according to the analysis,[6] they contain chains of PNP and POP defects. One expects that the values of $0.4$ eV $\leq E_m^{near} \leq 0.6$ eV obtained in our simulations may be related to mobile ion migration near the chains in these materials. Because of the disorder, the notion of vacancy and interstitial is no longer relevant. More detailed analysis of plausible structures relevant to the LiPON system remains to be investigated.

*duy@wfu.edu

†natalie@wfu.edu

[1] Y. A. Du and N. A. W. Holzwarth, Phys. Rev. B **76**, 174302 (2007).

[2] Y. A. Du and N. A. W. Holzwarth, J. Electrochem. Soc. **154**, A999 (2007).

[3] A. K. Ivanov-Shitz, V. V. Kireev, O. K. Mel'nikov, and L. N. Demainets, Crystallogr. Rep. **46**, 864 (2001).

[4] J. B. Bates, N. J. Dudney, G. R. Gruzalski, R. A. Zuhr, A. Choudhury, D. F. Luck, and J. D. Robertson, Solid State Ionics **53-56**, 647 (1992).

[5] J. B. Bates, N. J. Dudney, G. R. Gruzalski, R. A. Zuhr, A.

Choudhury, D. F. Luck, and J. D. Robertson, J. Power Sources **43-44**, 103 (1993).

[6] B. Wang, B. S. Kwak, B. C. Sales, and J. B. Bates, J. Non-Cryst. Solids **183**, 297 (1995).

[7] B. Wang, B. C. Chakoumakos, B. C. Sales, B. S. Kwak, and J. B. Bates, J. Solid State Chem. **115**, 313 (1995).

[8] X. Yu, J. B. Bates, J. G. E. Jellison, and F. X. Hart, J. Electrochem. Soc. **144**, 524 (1997).

[9] Y.-W. Hu, I. D. Raistrick, and R. A. Huggins, J. Electrochem. Soc. **124**, 1240 (1977).

[10] W. H. Baur and T. Ohta, J. Solid State Chem. **44**, 50 (1982).

[11] J. F. Whitacre and W. C. West, Solid State Ionics **175**, 251

(2004).

[12] P. Hohenberg and W. Kohn, Phys. Rev. **136**, B864 (1964).

[13] W. Kohn and L. J. Sham, Phys. Rev. **140**, A1133 (1965).

[14] J. P. Perdew and Y. Wang, Phys. Rev. B **45**, 13244 (1992).

[15] Quantum-ESPRESSO is a community project for high-quality quantum-simulation software, based on density functional theory, and coordinated by Paolo Giannozzi. See http://www.pwscf.org and http://www.quantum-espresso.org

[16] D. Vanderbilt, Phys. Rev. B **41**, 7892 (1990); the USPP code is available from the web site http://www.physics.rutgers.edu/~dhv/uspp/

[17] N. A. W. Holzwarth, A. R. Tackett, and G. E. Matthews, Comput. Phys. Commun. **135**, 329 (2001); available from the web site http://pwpaw.wfu.edu

[18] A. R. Tackett, N. A. W. Holzwarth, and G. E. Matthews, Comput. Phys. Commun. **135**, 348 (2001); available from the web site http://pwpaw.wfu.edu

[19] P. E. Blöchl, Phys. Rev. B **50**, 17953 (1994).

[20] N. A. W. Holzwarth, G. E. Matthews, R. B. Dunning, A. R. Tackett, and Y. Zeng, Phys. Rev. B **55**, 2005 (1997).

[21] A. Kokalj, J. Mol. Graphics Modell. **17**, 176 (1999).

[22] OPENDX—the open source software project based on IBM's Visualization Data Explorer—is available from the web site http://www.opendx.org

[23] H. Jónsson, G. Mills, and K. W. Jacobsen, in *Classical and Quantum Dynamics in Condensed Phase Simulations*, edited by B. J. Berne, G. Ciccotti, and D. F. Coker (World Scientific, Singapore, 1998), pp. 385–404.

[24] G. Henkelman, B. P. Uberuaga, and H. Jónsson, J. Chem. Phys. **113**, 9901 (2000).

[25] G. Henkelman and H. Jónsson, J. Chem. Phys. **113**, 9978 (2000).

[26] *International Tables for Crystallography*, Space-Group Symmetry Vol. A, 5th ed., edited by T. Hahn (Kluwer, Dordrecht, 2002).

[27] J. Zemann, Acta Crystallogr. **13**, 863 (1960).

[28] O. V. Yakubovich and V. S. Urusov, Crystallogr. Rep. **42**, 261 (1997).

[29] C. Keffer, A. Mighell, F. Mauer, H. Swanson, and S. Block, Inorg. Chem. **6**, 119 (1967).

[30] In order to simplify the comparison between the PNP and POP structures, we used the same stoichiometry of $Li_{3-1/16}PO_{4-2/16}N_{1/16}$ for both simulations. For the POP structures, we substituted a N ion for O far from the defect site, so that the results would not appreciably affected by N. The N contributions to the densities of states were omitted from the plot for the POP defect in Fig. 5. The N contribution could also affect the total energy estimate, but we expect the corresponding energies given in Table I to vary by no more than 0.2 eV.

[31] See EPAPS Document No. E-PRBMDO-78-100837 for additional structural diagrams, densities of states, and electron-density contour plots. For more information on EPAPS, see http://www.aip.org/pubservs/epaps.html.

[32] T. M. Alam and J. M. Segall, J. Mol. Struct.: THEOCHEM **674**, 167 (2004).

[33] There are two other possible N placements for this interstitial Li-ion site, which have higher energies of 0.01 and 0.21 eV.

[34] J. M. Léger, J. Haines, C. Chateau, G. Bocquillon, M. W. Schmidt, S. Hull, F. Gorelli, A. Lesauze, and R. Marchand, Phys. Chem. Miner. **28**, 388 (2001).

[35] D. Stachel, Acta Crystallogr., Sect. C: Cryst. Struct. Commun. **51**, 1049 (1995).

[36] E. H. Arbib, B. Elouadi, J. P. Chaminade, and J. Darriet, J. Solid State Chem. **127**, 350 (1996).

[37] J. C. Guitel and I. Tordjman, Acta Crystallogr., Sect. B: Struct. Crystallogr. Cryst. Chem. **32**, 2960 (1976).

[38] A. Daidouh, M. L. Veiga, C. Pico, and M. Martinez-Ripoll, Acta Crystallogr., Sect. C: Cryst. Struct. Commun. **53**, 167 (1997).

[39] M. R. Reidmeyer and D. E. Day, J. Non-Cryst. Solids **181**, 201 (1995).

[40] A. Le Sauze, L. Montagne, G. Palavit, and R. Marchand, J. Non-Cryst. Solids **293-295**, 81 (2001).

[41] D. Tranqui, R. D. Shannon, H. Y. Chen, S. Iijima, and W. H. Baur, Acta Crystallogr., Sect. B: Struct. Crystallogr. Cryst. Chem. **35**, 2479 (1979).

[42] B. H. W. S. de Jong, D. Ellerbroek, and A. L. Spek, Acta Crystallogr., Sect. B: Struct. Sci. **50**, 511 (1994).

[43] R. Hoppe, K. Bernet, and A. Möller, Z. Anorg. Allg. Chem. **629**, 1285 (2003).

[44] M. Miyachi, H. Yamamoto, H. Kawai, T. Ohta, and M. Shirakata, J. Electrochem. Soc. **152**, A2089 (2005).

[45] Q. Sun, B. Zhang, and Z.-W. Fu, Appl. Surf. Sci. **254**, 3774 (2008).

[46] C. H. Choi, W. I. Cho, B. W. Cho, H. S. Kim, Y. S. Yoon, and Y. S. Tak, Electrochem. Solid-State Lett. **5**, A14 (2002).

[47] W.-Y. Liu, Z.-W. Fu, C.-L. Li, and Q.-Z. Qin, Electrochem. Solid-State Lett. **7**, J36 (2004).

[48] W. C. West, J. F. Whitacre, and J. R. Lim, J. Power Sources **126**, 134 (2004).

[49] P. E. Stallworth, F. Vereda, S. G. Greenbaum, T. E. Haas, P. Zerigian, and R. B. Goldner, J. Electrochem. Soc. **152**, A516 (2005).

[50] Y. Hamon, A. Douard, F. Sabary, C. Marcel, P. Vinatier, B. Pecquenard, and A. Levasseur, Solid State Ionics **177**, 257 (2006).

[51] F. Muñoz, A. Durán, L. Pascual, L. Montagne, B. Revel, and A. C. M. Rodrigues, Solid State Ionics **179**, 574 (2008).

[52] This does not include some films reported in the literature that either did not report the stoichiometry or reported a non-neutral stoichiometry.